Journal of Industrial Intelligence
https://www.acadlore.com/journals/JII

Aerodynamic Performance of High-Speed Maglev Trains Under Crosswind Conditions: A Computational Simulation Study

Yifan Yan[1], Yuhang Zhao[2], Yuze Zhang[3], Meiqi Wang[3*]

[1] CRRC Industrial Research Institute Co., Ltd, 100070 Beijing, China
[2] CRRC Tangshan Co., Ltd, 064000 Tangshan, China
[3] School of Mechanical Engineering, Shijiazhuang Tiedao University, 050043 Shijiazhuang, China

* Correspondence: Meiqi Wang (wangmeiqi@stdu.edu.cn)

Received: 11-08-2023 **Revised:** 12-14-2023 **Accepted:** 12-22-2023

Citation: Y. F. Yan, Y. H. Zhao, Y. Z. Zhang, and M. Q. Wang, "Aerodynamic performance of high-speed maglev trains under crosswind conditions: A computational simulation study," *J. Ind Intell.*, vol. 1, no. 4, pp. 241–251, 2023. https://doi.org/10.56578/jii010405.

Abstract: In the realm of ground transportation, high-speed maglev trains stand out due to their exceptional stability, rapid velocity, and environmental benefits, such as low pollution and noise. However, the aerodynamic challenges faced by these lightweight, high-velocity trains significantly impact their safety and comfort, making aerodynamics a critical aspect in their design. This research delves into the dynamic aerodynamic behavior of high-speed maglev trains in the presence of crosswinds. A simulation analysis was conducted on a simplified model of a three-car maglev train, with an established aerodynamic model for the train and track beam in crosswind scenarios. The study employed three-dimensional, steady-state, incompressible $N-S$ equations, complemented by a $k-\varepsilon$ dual-equation turbulence model. The finite volume method was utilized to assess the flow field structure around the train and the pressure distribution on its surface under varying combinations of train speed and wind velocity. The investigation summarized the patterns and trends in aerodynamic loads across diverse conditions. Results demonstrate that at a speed of 600 km/h, the tail car is subjected to the highest aerodynamic drag, while the head car bears the maximum lateral force and overturning moment. As crosswind speeds increase from 5 m/s to 20 m/s, the tail car exhibits the largest increment in drag, reaching 16.6 kN. The front car shows the most significant rise in lateral force and overturning moment, measured at 34.11 kN and 52.45 kN·m, respectively. It is observed that the behavior of aerodynamic forces at lower and medium speeds aligns fundamentally with the patterns noted at higher speeds.

Keywords: Crosswind; Maglev train; Aerodynamics; Operation safety; Stability

1 Introduction

The impact of crosswinds on the operational stability and safety of trains is a subject of considerable significance. Under strong crosswind conditions, the operational dynamics of maglev trains exhibit substantial deviations compared to scenarios devoid of crosswind, a phenomenon referred to as the crosswind effect. This effect not only complicates the control of trains but also poses risks of fatigue damage to the train body and track structures, potentially leading to significant alterations in train dynamics, such as derailment or overturning. Traditional rail-type trains, usually heavier, often underestimate the influence of aerodynamic lift. In contrast, maglev trains, being relatively lighter and closer to the ground, demonstrate more pronounced aerodynamic ground effects than rail-type trains. Thus, addressing aerodynamic challenges induced by crosswinds is essential in the development of high-speed maglev trains. Ensuring the dynamic performance of high-speed maglev trains in crosswind conditions is vital for their safe operation and for preventing crosswind-induced accidents. Existing research on maglev train aerodynamics predominantly focuses on speeds between 200 km/h and 350 km/h; however, studies on high-speed maglev trains, particularly those addressing speeds beyond this range, are limited but advancing globally.

In wind tunnel experiments, Ma [1] explored the tunnel pressure wave and aerodynamic characteristics of maglev trains at 600 km/h. Chen [2] investigated the pressure wave and aerodynamic performance of high-speed maglev trains in the open air. Huang [3] researched on maglev train aerodynamics predominantly focuses on speeds between 200 km/h and 350 km/h. Researchers from the University of Birmingham, including Baker et al. [4–7], conducted studies on the aerodynamic performance of high-speed trains under strong wind conditions, analyzing variations in

aerodynamic forces and moments and examining aerodynamic characteristics in depth. Soper et al. [8] simulated scenarios involving passenger trains and atmospheric boundary layers relative to the road surface in wind tunnel experiments, deriving aerodynamic forces and moments on trains under crosswind loads and identifying patterns in aerodynamic characteristics. Flynn et al. [9] extended their research to the changes in aerodynamic characteristics during train operation. Swedish researchers Krajnovic et al. [10–12] were among the first to apply large eddy simulation to train aerodynamics, using both simulation and wind tunnel experiments. Their findings affirmed the applicability of large eddy simulation for external flow field modeling of trains and for studying train dynamics under crosswind conditions. Thomas et al. [13] conducted exemplary experiments on the aerodynamic characteristics of high-speed trains under crosswinds, employing hydraulic devices on trains to simulate crosswind aerodynamic loads, with subsequent comparisons to simulation data revealing a high degree of correlation.

Investigations by Misu and Ishihara [14] focused on the dynamic and safety performance of trains navigating complex terrains under strong crosswind conditions. A synergistic approach combining numerical simulations and field measurements was utilized, employing time series methods for predicting maximal wind speeds and wind direction angles. This methodology enabled the determination of safe operating speeds for high-speed trains under severe wind conditions. The Italian research team, led by Tomasini and Cheli [15], examined the effects of crosswinds on the aerodynamic load coefficients and aerodynamic coefficients of high-speed trains across various road conditions. Their analysis contributed to the design of train fronts and roofs optimized for harsh wind conditions, enhancing the safety of high-speed trains in crosswind environments. Cheli et al. [16] applied when the train body forms a 90-degree angle with the crosswind inflow, the drag coefficient is associated with the Reynolds number. Catanzaro et al. [17] applied fluid dynamics simulation software to model the crosswind stability of the ETR series high-speed trains in both static and dynamic states, comparing their aerodynamic performance with wind tunnel experimental data. Findings revealed a closer alignment of static models with experimental outcomes. Liu et al. [18] from Central South University utilized the sliding mesh technique to simulate the uniform acceleration process of trains in crosswind environments, calculating the root mean square values of unsteady coefficients during the uniform motion phase and comparing these with wind tunnel experiment results. Furthermore, Imai et al. [19] conducted comprehensive studies on train accidents in Japan under severe wind conditions, including strong crosswinds. They proposed the theoretical feasibility of windbreak wall structures for effectively reducing accidents in strong crosswind environments. From South Korea, Kim et al. [20] introduced a novel theoretical formula for train derailment under crosswind conditions, which underwent comparison and validation against numerical simulation results from conventional derailment formulas in multibody dynamics software.

The development of higher-speed maglev trains is thus identified as a progressive trend. Pursuing aerodynamic research at speeds of 600 km/h and analyzing the high-speed performance of maglev trains under aerodynamic forces hold significant value for consolidating the technological foundations of maglev technology and paving the way for the next generation of maglev trains.

2 Methodology

2.1 Geometric Model

In analyzing the composition and modeling of maglev vehicles, the focus was placed on the train body and the suspension frame, encompassing detailed structural outlines, dimensions, and interconnections of components. The process of geometric modeling involved transformational adjustments to preserve the principal external characteristics of the entire train body. These adjustments included the elimination of interconnections among the three sections of the train body, the integration of the train body with the suspension frame, and a substantial simplification of the suspension frame itself. This simplification process entailed the removal of elements such as suspension and guidance magnets and the unification of the entire train's suspension frame. Surface smoothing and filling were performed on the suspension frame, as depicted in Figure 1.

2.2 Computational Domain and Boundary Conditions

To effectively simulate the aerodynamic characteristics of each car of the maglev train, while maintaining a balance between computational accuracy and efficiency, a formation comprising the head car, a middle car, and the tail car was modeled. This approach was based on the consistent structure and unchanging cross-section of the train's middle cars. The geometric model was arranged to reflect the actual train configuration, with the cars interconnected by fully enclosed windshields. The overall length of the train model approximated 81 meters. A suitable computational domain was determined: the area preceding the train longitudinally should extend at least twice the train's width, while the area at the rear should span more than twice the total train length. The domain's width and height were set to be at least 5-6 times the train's width. Considering the symmetrical nature of the train, a half-model approach was adopted to reduce computational demands, resulting in a final computational domain dimension of 300 m $\times$ 60 m $\times$ 42 m. Reverse modeling involved extracting the train body structure from the entire domain, leaving only regions where airflow would occur, thereby facilitating grid division.

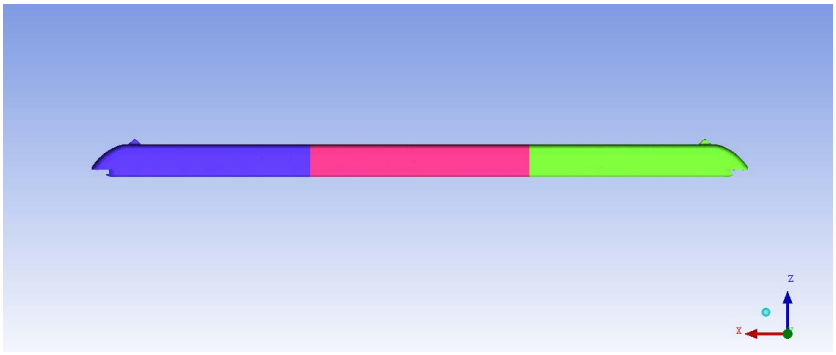

(a) Side view of the entire train

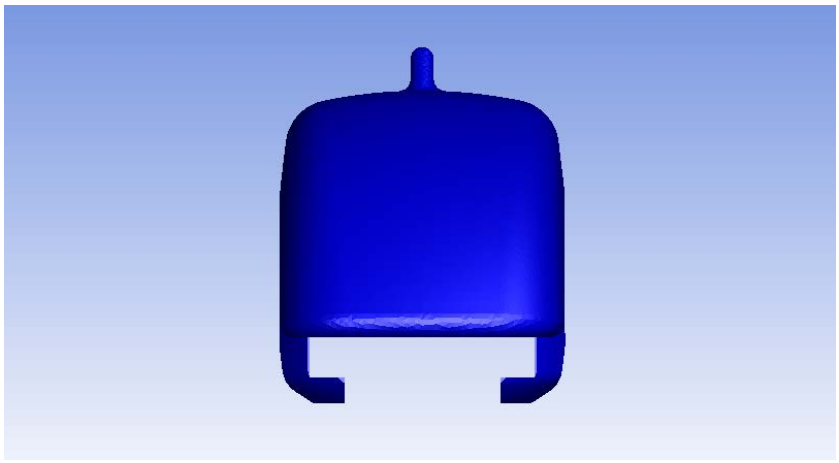

(b) Front detail of the head car

Figure 1. Simplified three-dimensional geometric model of the maglev train

2.3 Computational Grid

In addressing the complexity of the train's structure, tetrahedral grids were employed for segmentation. The flow characteristics of each region were meticulously considered, leading to the determination of appropriate cell sizes and expansion ratios through extensive preliminary trials. For the train body, the largest grid size was established at 0.1 m, and for the track beam, at 0.4 m. The comprehensive computational grid is illustrated in Figure 2, with a detailed grid diagram of the maglev train and bridge presented in Figure 3. The grid quantity and quality underwent thorough evaluation, initiating with an overall optimization to enhance grid quality beyond a threshold of 0.24. Subsequent localized smoothing procedures were applied. Given that adjustments in the dimensions of each tetrahedral grid influence the quality of adjacent grids, the smoothing intensity was methodically reduced from critical to peripheral grid zones, culminating in an overall grid quality exceeding 0.3. Additionally, the division of boundary layer grids was undertaken to more accurately depict the influence of the boundary layer on the train body surface. The initial layer of the boundary grid was set to a height of 2 mm, with a Y^+ value of approximately 300, comprising 10 layers as depicted in Figure 4. The final tally of grids reached 11,459,871. The smallest grid volume measured 1.907218e-07m^3, with no negative grids present. The minimum orthogonality quality recorded was 3.38614e-02, the maximum skewness 9.66139e-01, and the maximum aspect ratio 1.78387e+02. The integration of boundary layer grids discernibly imposed limitations on the overall grid quality.

2.4 Solver Configuration

In the computation of aerodynamic performance, a three-dimensional steady-state approach was selected to optimize computational resource utilization. Given that the maximum Mach number during train operation approximates 0.3, the flow was treated as incompressible. The standard $k-\varepsilon$ turbulence model, along with standard wall functions, was employed to effectively capture flow dynamics within the boundary layer. The asymmetrical nature of the flow field under crosswind conditions necessitated the use of full-scale models. The computational domain was dimensioned at 300 m $\times$ 120 m $\times$ 42 m, as depicted in Figure 5. In the FLUENT software, the Semi-Implicit Method for Pressure Linked Equations (SIMPLEC) algorithm, encompassing both the standard SIMPLEC and SIMPLE-Consistent algorithms, was utilized. As the model did not require the activation of additional laminar flow

models, pressure-velocity coupling was confined to enhance the convergence of computations. Consequently, the standard format for coupling pressure and velocity was set to SIMPLEC, with the pressure correction relaxation factor designated at 1.0. For spatial discretization, gradients were configured to the green-gauss node based method. Pressure and momentum were calculated using a second-order format, while turbulent kinetic energy and turbulence dissipation were processed in a first-order upwind format to facilitate relatively convergent outcomes.

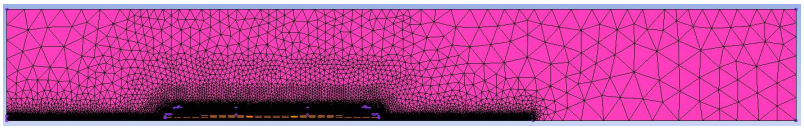

Figure 2. Schematic of the overall computational grid

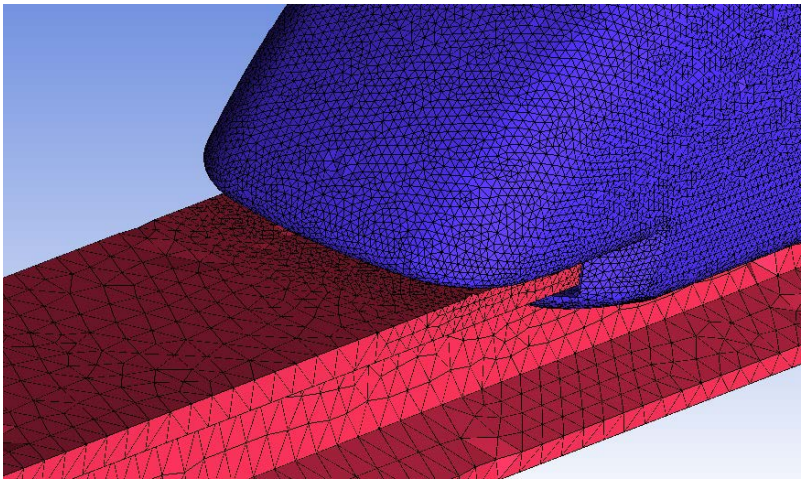

Figure 3. Partial grid diagram of the maglev train and track beam

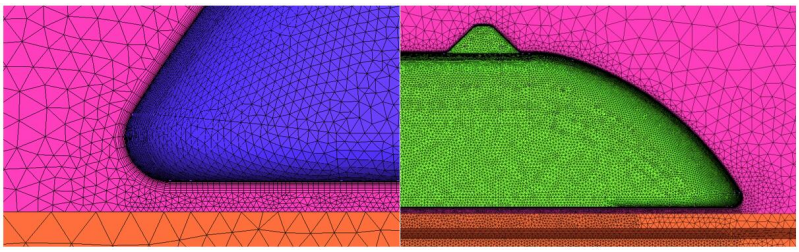

Figure 4. Schematic of the train body grid and boundary layer grid

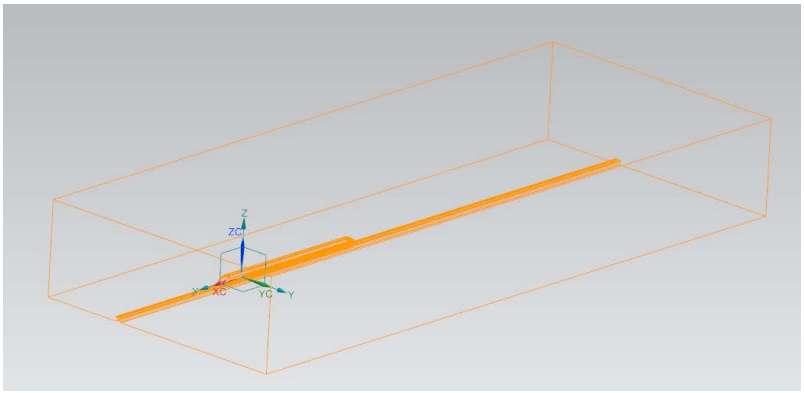

Figure 5. Computational domain for crosswind stability model

3 Computational Method

3.1 Aerodynamic Load Classification for High-Speed Maglev Trains

In the realm of high-speed travel, maglev trains encounter six principal types of aerodynamic loads induced by airflow: aerodynamic drag, lift, lateral force, overturning moment, pitching moment, and yawing moment. Given the significant impact on train dynamics and computational considerations, the focus of the analysis is predominantly on aerodynamic drag, lateral force, and overturning moment.

3.1.1 Aerodynamic drag analysis

Air resistance experienced by high-speed trains arises from two distinct types of stress. Wall shear stress, tangential to the train's surface, contributes to friction drag, whereas pressure stress, perpendicular to the surface, results in pressure drag. The aggregate drag is the cumulative effect of both friction and pressure drag along the airflow direction. Due to practical challenges in directly calculating the wind's shear stress on the train body, total drag is deduced using the subsequent equation:

$$F_D = \frac{1}{2} C_D \rho V^2 A \tag{1}$$

where, C_D signifies the drag coefficient, encapsulating intricate parameters like the effects of the object's geometric shape or the state of flow. This coefficient is ascertainable through wind tunnel experiments and numerical simulations. ρ represents the fluid density, V denotes the stable and uniform free flow velocity, and A is the reference area, which varies based on the drag coefficient. Hence, for the streamlined body of a maglev train, A typically pertains to the planar area.

3.1.2 Analysis of lateral force

The lateral force acting on the train, primarily induced by crosswinds, is fundamentally a manifestation of fluid resistance. In assessing the lateral force for the maglev train's body, A in Eq. (1) accounts for the train's projected area in the crosswind direction.

The lateral force exerted on the train body predominantly comprises pressure drag, attributable to the pressure differential between the windward and leeward sides. As the crosswind interacts with the train surface, acceleration occurs, leading to a reduction in pressure along the flow direction and the formation of a beneficial pressure gradient, as depicted in Figure 6. The boundary layer of the fluid detaches on the leeward side, creating a low-pressure area known as the separation zone, consequently generating resistance. This fluid separation further induces vortex shedding, potentially causing detrimental vibrations and instability. Notably, when the train body forms a 90-degree angle with the crosswind inflow, the drag coefficient is associated with the Reynolds number. Theoretically, an increase in crosswind speed markedly elevates the pressure drag on both sides of the train body.

Figure 6. Pressure gradient changes on the train body surface under crosswind

3.1.3 Aerodynamic moments

Aerodynamic moments, encompassing overturning, pitching, and yawing moments, are rotational effects resulting from aerodynamic forces exerted on the train body. This study designated the X, Y, and Z axes at the centers of gravity of the three train sections as axes for calculating moments. An exploration was conducted to understand the relationship between aerodynamic forces and moments under varying crosswind and train speeds.

4 Result Analysis

4.1 Flow Field Analysis of High-Speed Maglev Trains

The flow field analysis for high-speed maglev trains encompasses examining the pressure conditions on the train surface and the flow field distribution around the train body. To enhance the clarity and precision of the analysis, the

model was segmented into three distinct sections: the head car, the middle car, and the tail car. The study employed train speeds of 350 km/h and crosswind speeds of 15 m/s.

4.1.1 Aerodynamic drag

The investigation into the aerodynamic drag revealed that the pressure distribution on the surface of high-speed maglev trains under crosswind conditions varied significantly from those operating without crosswinds. As demonstrated in Figure 7, the highest pressure, characterized as positive pressure, was observed at the nose cone of the head car. The crosswind effect caused the pressure stagnation point to shift towards the windward side of the tip. Similarly, the nose cone of the tail car displayed relatively high positive pressure, with regions of negative pressure developing on parts of its windward side. The windward side predominantly exhibited positive pressure, while the leeward side was chiefly subjected to negative pressure. Notably, although the head and tail cars share similar shapes, the pressured conditions on their windward and leeward sides contrasted significantly.

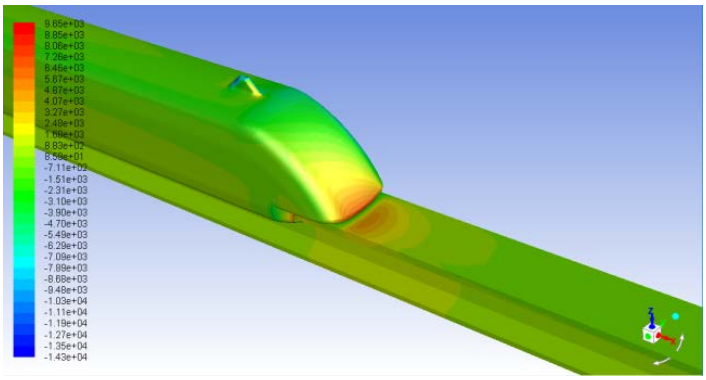

(a) Windward side pressure cloud diagram of the head car

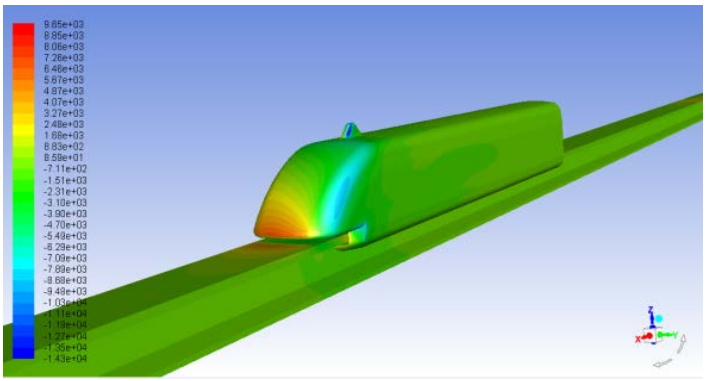

(b) Leeward side pressure cloud diagram of the head car

Figure 7. Surface pressure cloud diagram of the head car

4.1.2 Flow field characteristics around the train body in crosswinds

In order to ascertain the impact of crosswinds on the flow field surrounding the train body, six cross-sectional areas along the axial direction were selected for analysis. These sections, positioned perpendicularly to the train's axis, were determined based on axial coordinates. Given the notable influence of fluid dynamics on the aerodynamic performance of the head car, followed by the tail car, and with the middle car exhibiting the most stability, the chosen sections included two for the head car, as illustrated in Figure 8, two for the middle car, as shown in Figure 9, and two for the tail car, as depicted in Figure 10. The arrangement of these cross-sections of the train body is represented in Figure 8. The train and wind speeds utilized for this analysis were 350 km/h and 20 m/s, respectively.

In examining the aerodynamic forces acting on the head car of the high-speed maglev train, it was observed that the crosswind significantly influences the windward side, almost stagnating lateral airflow and resulting in predominantly positive pressure. This observation was made evident by the separation of the section with the highest positive pressure upon encountering the train body. A portion of the airflow was directed towards the train, while the remainder passed over the top, leading to an increase in velocity and predominantly negative pressure in most of the roof area. This effect caused the convergence of upper and lower air streams into vortices on the leeward side, developing backward over time. Consequently, a pressure differential force was exerted from the windward to the leeward side of the head car, aligning the lateral force direction with that of the crosswind.

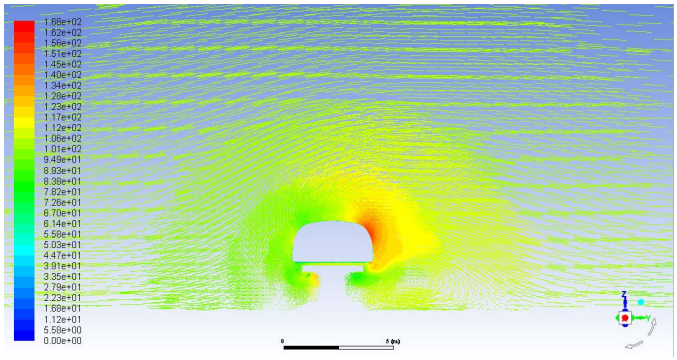

(a) Section one pressure cloud diagram of the head car

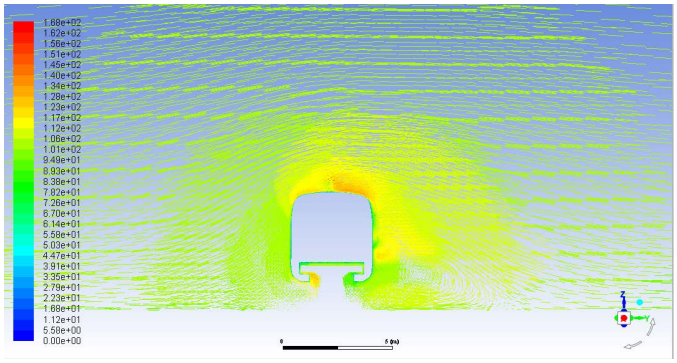

(b) Section two pressure cloud diagram of the head car

Figure 8. Velocity flow field at the head car interface of the high-speed maglev train

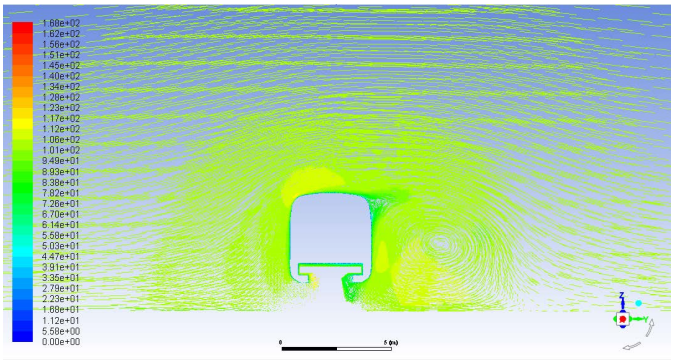

(a) Section one pressure cloud diagram of the middle car

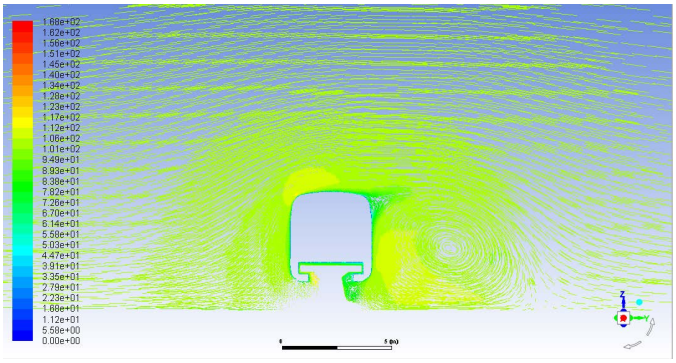

(b) Section two pressure cloud diagram of the middle car

Figure 9. Velocity flow field at the middle car interface of the high-speed maglev train

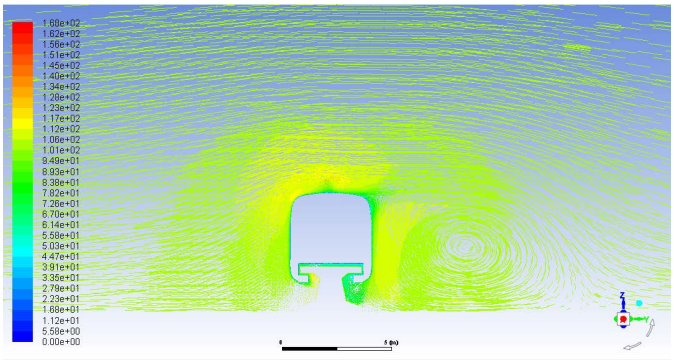

(a) Section one pressure cloud diagram of the tail car

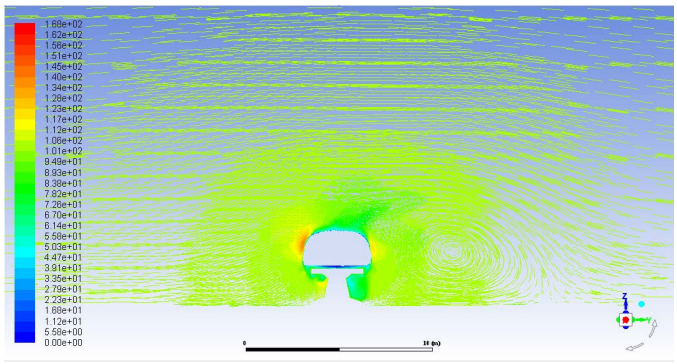

(b) Section two pressure cloud diagram of the tail car

Figure 10. Velocity flow field at the tail car interface of the high-speed maglev train

In contrast, the cross-sections of the middle car exhibited uniform inflow characteristics, pressure distribution, streamline distribution, and vortex shedding patterns. Positive pressure was maintained on the windward side, while the leeward side experienced negative pressure. Given the near-identical flow field characteristics and dimensions across each section, the aerodynamic performance of the middle car was noted to be relatively stable.

Regarding the tail car, a gradual increase in wind speed was noted on the windward side as it approached the nose, leading to a reduction in pressure on the leeward side. This phenomenon resulted in a lateral pressure differential force from the leeward to the windward side, thus establishing a direction for the lateral force that is opposite to the incoming crosswind.

4.2 Impact of Operating Speed on Aerodynamic Loads

The study considered high-speed maglev trains operating at velocities of 200 km/h, 400 km/h, and 600 km/h, and crosswind speeds varying from 5 m/s to 20 m/s. The macroscopic aerodynamic characteristics of the three distinct train segments under varying conditions were methodically compared.

4.2.1 Variation pattern in aerodynamic drag

Figure 11 illustrates that at 200 km/h, the head car encounters its maximum drag at a crosswind of 20 m/s. Conversely, at higher speeds of 400 km/h and 600 km/h, the peak drag is noted at a crosswind of 5 m/s. For both the middle and tail cars, the highest drag consistently occurs at a crosswind speed of 20 m/s. Over the speed range from 200 km/h to 600 km/h, a notable variation in maximum drag is observed: an increase of 21.26 kN for the head car, 9.86 kN for the middle car, and 47.09 kN for the tail car.

The tail car is seen to exhibit the most substantial absolute and relative increase in drag among the three segments. Under identical speed scenarios, the drag direction for the middle and tail cars is counter to the travel direction and escalates with wind speed. The head car's drag direction shift is in contrast to the other two segments; under conditions of low speed and high crosswind, the drag direction aligns with the travel direction. When maintaining a constant crosswind speed, an increase in train speed results in augmented drag for all three cars, with the tail car experiencing the most pronounced elevation. This pattern underscores the significant influence of crosswinds on the variation of drag, particularly for the tail car.

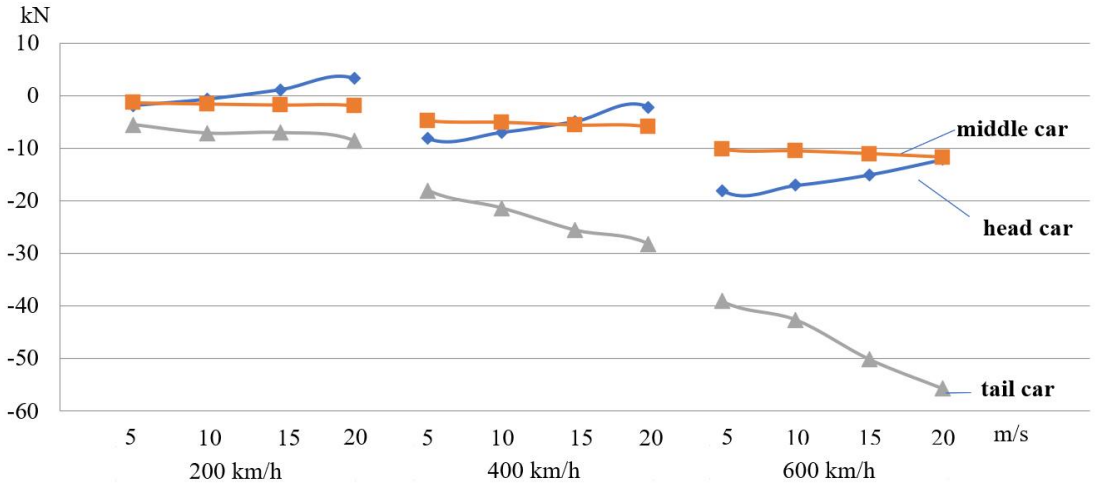

Figure 11. Pattern of aerodynamic drag

4.2.2 Variation pattern in lateral force

At varying operational speeds, each of the three train segments exhibited the highest lateral force at a crosswind speed of 20 m/s. The lateral force on the head car demonstrated a change of 28.58 kN from 200 km/h to 600 km/h, whereas the middle car and tail car showed changes of 15.29 kN and 13.26 kN, respectively.

As depicted in Figure 12, a pressure differential was observed from the leeward to the windward side of the tail car, a condition absent in the head and middle cars. This led to the lateral force direction on the head and middle cars being opposite to that of the tail car. With constant train speed, the lateral force experienced by all segments increased as the crosswind speed rose. The influence of crosswind speed on lateral force was markedly more pronounced than the effect of variations in train speed.

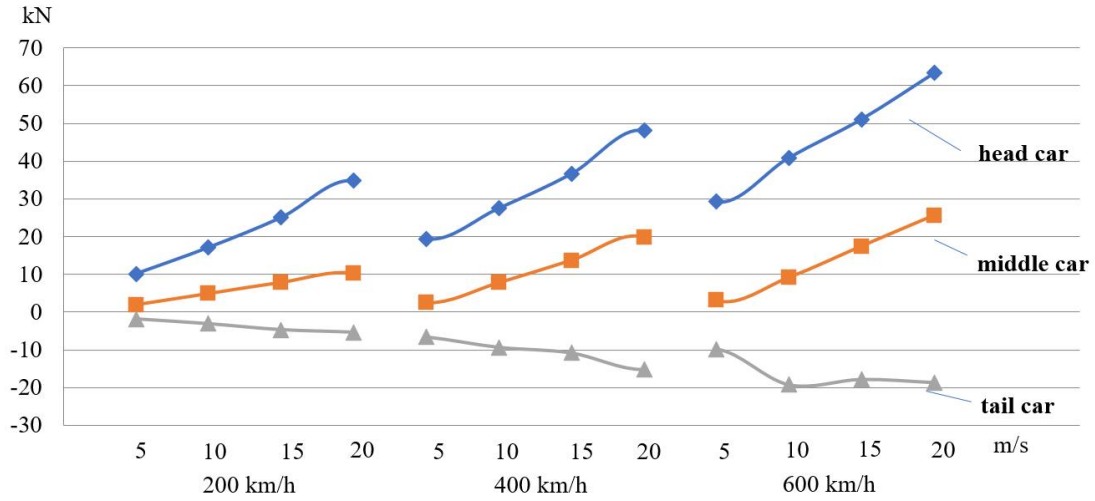

Figure 12. Pattern of lateral force

4.2.3 Variation pattern in overturning moment

As depicted in Figure 13, the pattern of change in the train body's overturning moment largely paralleled that of the lateral force. The peak overturning moments for the three train sections at varying speeds all occurred at a crosswind speed of 20 m/s. The head car's maximum overturning moment altered by 49.29 kN·m, the middle car by 15.29 kN·m, and the tail car by 13.26 kN·m from 200 km/h to 600 km/h. Notably, at 600 km/h, the augmentation in the head car's lateral force with an increase in crosswind speed was considerably more substantial than that observed in the middle and tail cars.

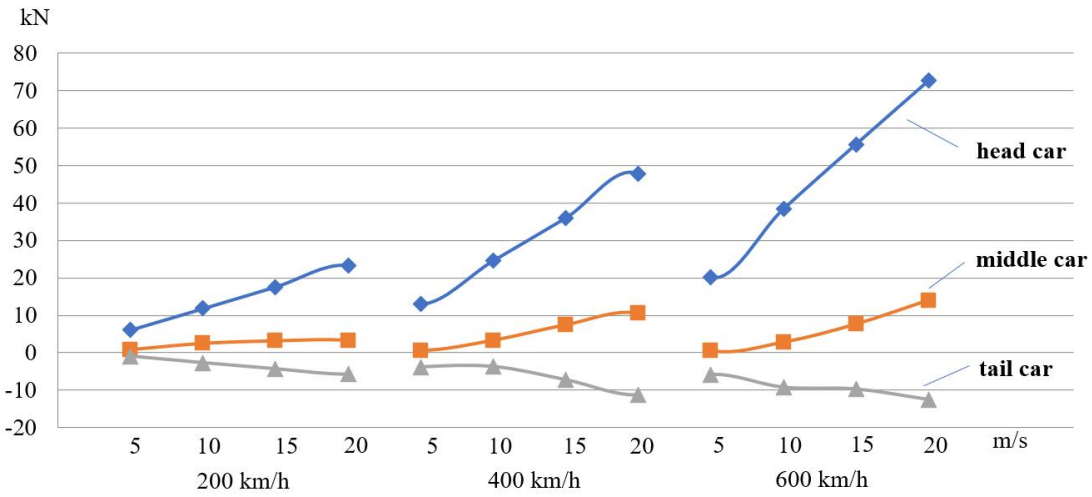

Figure 13. Pattern of overturning moment

5 Conclusions

The study conducted a comprehensive investigation into the aerodynamic performance of high-speed maglev trains at velocities up to 600 km/h and under crosswind speeds ranging from 5 to 20 m/s. It was determined that the aerodynamic efficiency of these trains is primarily influenced by the dynamics of the head and tail cars. An increase in either the train's velocity or the crosswind speed was observed to escalate the aerodynamic loads. A correlation analysis between the visual overviews from cloud diagrams and the quantified aerodynamic load data revealed a notable consistency.

In the realm of aerodynamic drag, the tail car, experiencing diminished fluid separation on its surface, thereby encountering more substantial viscous drag, endured greater drag compared to the head and middle cars. Under identical operational conditions, the difference in aerodynamic drag between the tail and head cars reached a maximum of 43.55 kN. In terms of lateral force, the head car displayed a considerable positive pressure gradient, contrasting with the minimal surface pressure on the middle car and the slight negative pressure gradient on the tail car. Consequently, the maximum lateral force was exhibited by the head car. Under similar conditions, the disparity in lateral force between the head and tail cars peaked at 44.7 kN. With the train speed held constant, the head car's lateral force underwent a maximum alteration of 28.58 kN as crosswind speed increased from 5 m/s to 20 m/s. Given the interrelation between lateral force and overturning moment, the head car's overturning moment was found to surpass that of the tail car.

Data Availability

The data used to support the research findings are available from the corresponding author upon request.

Conflicts of Interest

The authors declare no conflict of interest.

References

[1] D. B. Ma, "Study on pressure wave and aerodynamic characteristics of 600 km/h maglev train tunnel," mastersthesis, Lanzhou Jiaotong University, Lanzhou, 2018.

[2] J. X. Chen, "Study on pressure wave and aerodynamic performance of high-speed maglev train on line," mastersthesis, Lanzhou Jiaotong University, Lanzhou, 2018.

[3] Z. G. Huang, "Research on aerodynamics of ultra-high-speed maglev train," mastersthesis, Southwest Jiaotong University, Chengdu, 2018.

[4] C. J. Baker, J. Jones, F. Lopez-Calleja, and J. Munday, "Measurements of the cross wind forces on trains," *J. Wind Eng. Ind. Aerodyn.*, vol. 92, no. 7-8, pp. 547–563, 2004. https://doi.org/10.1016/j.jweia.2004.03.002

[5] C. J. Baker, "The flow around high speed trains," *J. Wind Eng. Ind. Aerodyn.*, vol. 98, no. 6, pp. 277–298, 2010. https://doi.org/10.1016/j.jweia.2009.11.002

[6] C. J. Baker, "The simulation of unsteady aerodynamic cross wind forces on trains," *J. Wind Eng. Ind. Aerodyn.*, vol. 98, no. 2, pp. 88–99, 2010. https://doi.org/10.1016/j.jweia.2009.09.006

[7] C. J. Baker, "A framework for the consideration of the effects of crosswinds on trains," *J. Wind Eng. Ind. Aerodyn.*, vol. 123, no. 2, pp. 130–142, 2013. https://doi.org/10.1016/j.jweia.2013.09.015

[8] D. Soper, C. J. Baker, and M. Sterling, "An experimental investigation to assess the influence of container loading configuration on the effects of a crosswind on a container freight train," *J. Wind Eng. Ind. Aerodyn.*, vol. 145, no. 4, pp. 304–317, 2015. https://doi.org/10.1016/j.jweia.2015.03.002

[9] D. Flynn, H. Hemida, and C. J. Baker, "On the effect of crosswinds on the slipstream of a freight train and associated effects," *J. Wind Eng. Ind. Aerodyn.*, vol. 156, no. 5, pp. 14–28, 2016. https://doi.org/10.1016/j.jweia.2016.07.001

[10] S. Krajnovic, "Large eddy simulation of flows around ground vehicles and other bluff bodies," *Philos. Trans. R. Soc. London, Ser. A*, vol. 367, no. 1899, pp. 2917–2930, 2009. https://doi.org/10.1098/rsta.2009.0021

[11] S. Krajnovic and L. Davidson, "Large-eddy simulation of the flow around a bluff body," *J. Am. Inst. Aeronaut Astronautics*, vol. 40, no. 5, pp. 927–936, 2002. https://doi.org/10.2514/2.1729

[12] S. Krajnovic, P. Ringqvist, K. Nakad, and B. Basara, "Large eddy simulation of the flow around a simplified train moving through a crosswind flow," *J. Wind Eng. Ind. Aerodyn.*, vol. 110, pp. 86–99, 2012. https://doi.org/10.1016/j.jweia.2012.07.001

[13] D. Thomas, M. Berg, S. Stichel, and B. Diedrichs, "Rail vehicle response to lateral carbody excitations imitating crosswind," *Proc. Inst. Mech. Eng. Part F: J. Rail Rapid Transit*, vol. 229, pp. 34–47, 2013. https://doi.org/10.1177/0954409713496765

[14] Y. Misu and T. Ishihara, "Prediction of frequency distribution of strong crosswind in a control section for train operations by using onsite measurement and numerical simulation," *J. Wind Eng. Ind. Aerodyn.*, vol. 174, pp. 69–79, 2018. https://doi.org/10.1016/j.jweia.2017.11.020

[15] G. Tomasini and F. Cheli, "Admittance function to evaluate aerodynamic loads on vehicles: Experimental data and numerical model," *J. Fluids Struct.*, vol. 38, no. 3, pp. 92–106, 2013. https://doi.org/10.1016/j.jfluidstructs.2012.12.009

[16] F. Cheli, S. Giappino, L. Rosa, G. Tomasini, and M. Villani, "Experimental study on the aerodynamic forces on railway vehicles in presence of turbulence," *J. Wind Eng. Ind. Aerodyn.*, vol. 12, no. 3, pp. 311–316, 2013. https://doi.org/10.1016/j.jweia.2013.09.013

[17] C. Catanzaro, F. Cheli, D. Rocchi, P. Schito, and G. Tomasini, "High-speed train crosswind analysis: CFD study and validation with wind-tunnel tests," in *The Aerodynamics of Heavy Vehicles III*. Springer, Cham, 2010, pp. 99–112.

[18] Z. C. Liu, D. Zhou, X. F. Liang, and J. Q. Niu, "Research on the aerodynamic characteristics of high-speed train accelerated operation under strong wind environment," *J. China Railway Soc.*, vol. 40, no. 7, pp. 40–46, 2018. https://doi.org/10.3969/j.issn.1001-8360.2018.07.006

[19] T. Imai, T. Fujii, K. Tanemoto, T. Shimamura, T. Maeda, H. Ishida, and Y. Hibino, "New train regulation method based on wind direction and velocity of natural wind against strong winds," *J. Wind Eng. Ind. Aerodyn.*, vol. 90, no. 12-15, pp. 1601–1610, 2002. https://doi.org/10.1016/s0167-6105(02)00273-8

[20] M. S. Kim, G. Y. Kim, H. T. Kim, and J. S. Koo, "Theoretical cross-wind speed against rail vehicle derailment considering the cross-running wind of trains and the dynamic wheel-rail effects," *J. Mech. Sci. Technol.*, vol. 30, no. 8, pp. 3487–3498, 2016. https://doi.org/10.1007/s12206-016-0708-2